

Computational Magnetohydrodynamics

Cavendish Laboratory, Department of Physics, J J Thomson Avenue, Cambridge. CB3 0HE

Abstract

Numerical simulation of Magnetohydrodynamic (MHD) equations is critical within plasma research. In this paper, the MHD system is solved using the 2nd order accurate MUSCL Hancock scheme together with an approximate HLLC Riemann Solver. Divergence cleaning is applied to the system to ensure physical and stable solutions can be obtained.

1. Introduction

Plasma is known as the fourth state of matter and formed when gas is being heated to certain temperature that atoms collide with each other and knock off their electrons. The main difference between a plasma and normal gas is the ability of plasma to sustain an electric current while normal gases are insulators. The dynamics of motion for plasma is complex as charge separation between ions and electrons results in electric fields, and the flow of charged particles give rise to current and magnetic fields.[7] Plasma can be characterised by density n and thermal energy KT_e . Given the wide density range of plasma (18 orders of magnitude from 1 to 10^{18} cm^{-3}), the matter finds application in many areas from the study of space physics to controlled thermonuclear fusion.[3]

Due to the requirement to solve large number of non linear partial differential equations over enormous ranges of time and space scales, computer simulation is well suited to study the nature of plasma science. The laboratory is currently working with Tokamak Energy to produce a full scale simulation of the nuclear fusion process within a Tokamak reactor. The fusion reaction between two hydrogen isotopes, deuterium(D) and tritium(T) is capable of releasing tremendous amounts of energy. In order to achieve fusion, three conditions must be full-filled: extremely high temperature on the order of 150 million degree Celsius; sufficient plasma

particle density to increase the frequency of collisions and sufficient plasma confinement time.[9]

Microscopically, although plasma consists of a group of particles interacting through known forces, methods of classical kinetic theory are insufficient to describe the plasma behaviour. Microscopic dynamics of plasma needs to be described as a study of many-body physics as the assumption of interaction forces can be represented by scarce binary encounters is not valid. In the presence of large magnetic field, the dynamics of plasma can be described by neglecting the local interactions and assuming the particles are moving independently, making it possible to model the plasma using hydrodynamic-like equations.[20]

From a macroscopic point of view, plasma interacting with magnetic field can be considered as a magnetohydrodynamic (MHD) fluid, which is an electrically conducting fluid subject to electromagnetic forces. In this paper, numerical simulation of compressible ideal MHD using high resolution method will be discussed. Test results are presented in 1-D and 2-D together with the effect of divergence cleaning.

This paper is structured as follow. Section 1 is the introduction. Section 2 provides an outline of the literature surrounding the subject. Section 3 details the governing

equations for ideal MHD system. Section 4 describes the numerical solver used in the paper to solve the system of equations. In section 5, results for several 1-D and 2-D tests have been presented. Section 6 discuss about some key aspects of the test results. Conclusions are presented in section 7.

2. Literature Review

Godunov's method has been widely used to solve hyperbolic partial differential equations with discontinuous solutions due to the ability to achieve high resolution at discontinuities and the robustness of the scheme. Upwind scheme for prescribing Godunov flux use wave propagation information contained in the differential equations, which can be obtained by solving a local 1-D Riemann problem in the direction normal to cell interface.[21] Hence, the essential ingredients for adopting Godunov's method is the solution of a Riemann problem, whether it is an exact or approximated solution. Riemann solvers can also be classified as complete or incomplete depending whether all the characteristic fields present in the exact Riemann problem are being included in the wave model. For solving MHD equations, exact Riemann solvers exist but it is recognised to be too computationally expensive. As a result, approximate Riemann solvers which can sometimes be an incomplete solver have been developed for solving MHD equations.[12]

The Roe's approximate Riemann solver is one of the earliest solvers adopted for solving MHD by a number of authors including Brio and Wu[2], Dai and Woodward[4], Powell[17], Ryu and Jones[19]. However, this solver is complex and computationally expensive as it requires eigen-decomposition. In contrast, the scheme requires about 10 times more floating point operations per grid point per time step than the Lax-Wendroff scheme.[2] Furthermore, the solver does not preserve the positivity of the solution which can lead to complicated issue in MHD when gas pressure is much less than magnetic pressure.[12]

approximate Riemann solver that will yield positive solution if used with an appropriate choice of wavespeed bounds. This scheme assumes the solution is a wave configuration that consists of two waves separating three constant states. Wave speed estimates proposed by Davis and Einfeldt has enabled the approach to produce practical results of intercell flux. The HLL scheme, together with the wave speed estimate proposed by Einfeldt, is known as the HLLE solver.

The assumption of the two wave configuration in HLL and HLLE scheme can lead to inaccurate solutions as the solvers are too diffusive and unable to resolve contact discontinuities very well. Einfeldt has proposed the HLLM scheme as a modification to the HLLE scheme, in which the single intermediate state in the HLL approach is modified by linear distribution. The other approach to modify the single state HLL, HLLEM, uses a partial eigen-decomposition and adds anti-diffusion terms only to the linearly degenerated fields.

Toro et al. has presented a different approach to tackle the problem of intermediate wave by adopting a 3 wave model with 2 intermediate states in the Riemann problem solution. The assumption of intermediate left and right states having the same pressure and velocity is valid for the contact wave, hence the solver is named HLLC ("C" stands for Contact). Batten et al. has retained most of the HLLC solver and suggested to use Roe average for computing the wavespeed of the intermediate states.[21]

The HLL-type solvers discussed have been successfully applied to the MHD problems by several authors. Janhunen[11] considered a MHD system which allows for magnetic monopoles through the addition of a source term $-\mathbf{v} \nabla \cdot \mathbf{B}$ on the right-hand side of Faraday's Law. This can be solved using the HLL solver and discretising the source term in a specific manner. To obtain a more accurate solution, the scheme can be hybridised with a Roe solver while retaining its positivity. Wessenberg[22] modified the HHLEM by adding anti-diffusion terms to all waves except the two Alfvén waves.

Harten, Lax, and van Leer (HLL) has proposed an

Linde[13] has proposed a modified two-state HLL solver

using only geometric interpretations of the Rankine Hugoniot conditions in a properly re-scaled vector space of conserved variables. The algorithm developed is a general purpose Riemann solver which is independent of the specific details of the governing equations. Gurski[8] has extended the HLLC solver for gas dynamics to MHD and included an algorithm to guarantee the positivity of pressure and density without altering the wavespeed of the outermost waves. This is known as the "smoothed HLLC-MHD" scheme and can be considered as a variant of Linde's solver.

Miyoshi and Kusano[16] has developed the HLLD Riemann Solver ("D" stands for discontinuity) that can resolve isolated discontinuities formed in the MHD system. This scheme is developed based on the assumptions of normal velocity being constant over the Riemann fan and rotational discontinuities propagating with the Alfvén waves may be generated. Hence, the HLLD scheme is an approximate Riemann problem with four intermediate states separated by one entropy and two Alfvén waves.

Li[12] has proposed a solver which is an extension of the two-state HLLC construction to MHD equations. The derived set of HLLC intermediate states have been checked with the integral form of the conservation laws to ensure the consistency condition is satisfied. However, it has been recognised that this solver is more diffusive than a linearised method which considers all the intermediate waves and Roe's solver has been recommended if exact resolution is important. In this paper, the solver proposed by Li has been adopted to solve all the test cases.

Given the discrete divergence of the discrete curl is not exactly zero, violation of $\nabla \cdot \mathbf{B} = 0$ constraint usually increases with time. As this happens, unphysical system behaviours such as magnetic field lines having the wrong topologies and plasma transport being orthogonal to the magnetic field lines can be observed.[5] Powell[18] has developed an eight-wave Roe type approximate Riemann solver to solve the ideal MHD equations in their symmetrisable form. As pointed out by Godunov, the system can only be rendered symmetrisable by adding a factor of the constraint $\nabla \cdot \mathbf{B} = 0$ to each of the equations. Evans

and Hawley[6] have proposed the constrained transport (CT) approach which relies on a staggered formulation of the electric and magnetic field. This formulation consists of defining the hydrodynamic variables at the centres, magnetic field at cell interfaces and electric field at zone edges. One clear advantage of this method is its inherently divergence-free magnetic field. Dedner et al.[5] prescribes a hyperbolic equation which allows the divergence errors to be propagated to the boundary of the domain. In this paper, the method proposed by Dedner et al. has been adopted while solving the 2-D cases.

3. Mathematical Equations

3.1. Conservation Law for Ideal MHD

In the presence of magnetic field, the motion of plasma is affected by both the electrodynamics and hydrodynamic behaviour. The MHD equations describe the motion of plasma which is dominated by electric and magnetic fields instead of pressure changes. The system of equations can be greatly simplified by assuming non-relativistic and zero resistance to the flow of plasma, which results in the ideal MHD equations. Combining the fluid dynamical equations and Maxwell's equations of electrodynamics, the set of non linear hyperbolic equations for ideal MHD can be derived,

$$\frac{\partial \rho}{\partial t} + \nabla \cdot (\rho \mathbf{v}) = 0 \quad (1a)$$

$$\frac{\partial \rho \mathbf{v}}{\partial t} + \nabla \cdot \left[\rho \mathbf{v} \otimes \mathbf{v} + \left(p + \frac{1}{2} B^2 \right) \mathbf{I} - \mathbf{B} \otimes \mathbf{B} \right] = 0 \quad (1b)$$

$$\frac{\partial U}{\partial t} + \nabla \cdot \left[\left(U + p + \frac{1}{2} B^2 \right) \mathbf{v} - (\mathbf{v} \cdot \mathbf{B}) \mathbf{B} \right] = 0 \quad (1c)$$

$$\frac{\partial \mathbf{B}}{\partial t} + \nabla \cdot (\mathbf{B} \otimes \mathbf{v} - \mathbf{v} \otimes \mathbf{B}) = 0 \quad (1d)$$

together with the additional divergence constraint.

$$\nabla \cdot \mathbf{B} = 0 \quad (1e)$$

Here ρ is the density, $\mathbf{v} = (v_x, v_y, v_z)^T$ the flow velocity, $\mathbf{B} = (B_x, B_y, B_z)^T$ the magnetic field, $U = \rho \varepsilon + \frac{1}{2} \rho v^2 + \frac{1}{2} B^2$ the total energy, p the hydrodynamic pressure. For

completely ionised plasma, ideal gas law can be used to close the system of equations,

$$p = (\gamma - 1)\rho\varepsilon \quad (2)$$

with adiabatic exponent $\gamma > 1$ [5]. In this paper, $\gamma = 5/3$ is used in all the test cases unless mentioned specifically.

3.2. 1-D Ideal MHD

Given the basis of numerical method used to solve the MHD system only considers one dimensional equations, derivatives and Riemann problem, the evolution equations need to be written in the following form.[15]

$$\frac{\partial \mathbf{u}}{\partial t} + \frac{\partial \mathbf{f}(\mathbf{u})}{\partial x} + \frac{\partial \mathbf{g}(\mathbf{u})}{\partial y} + \frac{\partial \mathbf{h}(\mathbf{u})}{\partial z} = 0 \quad (3)$$

Here \mathbf{u} is the conserved variable, $\mathbf{f}(\mathbf{u})$, $\mathbf{g}(\mathbf{u})$, $\mathbf{h}(\mathbf{u})$ are the flux functions in x, y, z directions respectively.

The standard conservation form in equations (1a) - (1d) can be written in 1-D prior applying numerical methods to solve them. While writing the flux functions in x direction, y and z components do not vanish while writing the equations in 1-D as non-zero B_y will evolve and feed back into the momentum and energy equations. However, $\frac{\partial B_x}{\partial t} = 0$ while writing the equations in x-direction.

$$\frac{\partial}{\partial t} \begin{bmatrix} \rho \\ \rho v_x \\ \rho v_y \\ \rho v_z \\ B_x \\ B_y \\ B_z \\ E \end{bmatrix} + \frac{\partial}{\partial x} \begin{bmatrix} \rho v_x \\ \rho v_x^2 + p + \frac{1}{2}B^2 - B_x^2 \\ \rho v_x v_y - B_x B_y \\ \rho v_x v_z - B_x B_z \\ 0 \\ B_y v_x - B_x v_y \\ B_z v_x - B_x v_z \\ (E + p + \frac{1}{2}B^2)v_x - B_x(\mathbf{v} \cdot \mathbf{B}) \end{bmatrix} = 0 \quad (4)$$

For solving MHD system greater than 1-D, flux functions in y and z directions can be written in the similar form as (4) with $\frac{\partial B_y}{\partial t} = 0$ and $\frac{\partial B_z}{\partial t} = 0$ respectively.

3.3. MHD Wave Speeds

The eigenvalues computed from the primitive variable form can be used to identify the wave speeds for an ideal

MHD system. Three acoustic waves can be determined, the Alfvén speed C_a , the slow and fast magneto-acoustic speeds, C_{sl} and C_f .

$$c_a = \frac{B}{\sqrt{\rho}} \quad (5)$$

$$c_{f,sl} = \sqrt{\frac{1}{2} \left[c_s^2 + c_a^2 \pm \sqrt{(c_s^2 + c_a^2)^2 - 4 \frac{c_s^2 B_x^2}{\rho}} \right]} \quad (6)$$

Here C_s is the speed of sound,

$$c_s = \sqrt{\frac{p\gamma}{\rho}} \quad (7)$$

4. Numerical Solver

4.1. HLL and HLLC Riemann Solver

The HLL and HLLC approximate Riemann solvers will be discussed in this section to ease the following derivation of a HLLC solver for MHD. The HLL solver is a two wave model which requires estimates for the fastest wave speeds emerging from contact discontinuity. As shown in section 4, the MHD equations can be written as

$$\frac{\partial \mathbf{u}}{\partial t} + \nabla \cdot \mathbf{F}(\mathbf{u}) = 0. \quad (8)$$

The discretised form of (8) using finite volume method can be written as

$$\mathbf{u}_i^{n+1} = \mathbf{u}_i^n - \frac{\Delta t}{\Delta x} (\mathbf{f}_{i+1/2}^n - \mathbf{f}_{i-1/2}^n). \quad (9)$$

Here $\mathbf{f}_{i\pm 1/2}^n$ is the inter-cell flux which governs the amount of materials entering or leaving the cell.

Constructing a Riemann problem along the x-direction with piece-wise constant left and right initial states ($t=0$) give

$$\mathbf{u}(x, 0) = \begin{cases} \mathbf{u}_L, & \text{if } x < 0 \\ \mathbf{u}_R, & \text{if } x > 0 \end{cases} \quad (10)$$

Using the HLL approach, the approximated Riemann solution can be obtained as

$$\mathbf{u}_{HLL} = \begin{cases} \mathbf{u}_L, & \text{if } S_L > 0 \\ \mathbf{u}^*, & \text{if } S_L \leq 0 \leq S_R \\ \mathbf{u}_R, & \text{if } S_R < 0 \end{cases} \quad (11)$$

Here the S_L and S_R are the fastest wave speeds for the left and right states. The intermediate subsonic state u^* can be calculated using

$$\mathbf{u}^* = \frac{S_R \mathbf{u}_R - S_L \mathbf{u}_L - (\mathbf{f}_R - \mathbf{f}_L)}{S_R - S_L} \quad (12)$$

where $f_L = f(u_L)$ and $f_R = f(u_R)$. Note that for the intermediate flux $f_{HLL} \neq f(u_{HLL})$ and must be computed using

$$\mathbf{f}_{HLL} = \frac{S_R \mathbf{f}_L - S_L \mathbf{f}_R + S_L S_R (\mathbf{u}_R - \mathbf{u}_L)}{S_R - S_L}. \quad (13)$$

The HLLC solver is a three wave model with the addition of a contact wave onto the existing two waves in HLL. This results in two intermediate states \mathbf{u}_L^* and \mathbf{u}_R^* , separated by an interface travelling at speed S^* . The HLLC approximate Riemann solution is

$$\mathbf{u}_{HLLC}(x, t) = \begin{cases} \mathbf{u}_L, & \text{if } \frac{x}{t} \leq S_L \\ \mathbf{u}_L^*, & \text{if } S_L \leq \frac{x}{t} \leq S^* \\ \mathbf{u}_R^*, & \text{if } S^* \leq \frac{x}{t} \leq S_R \\ \mathbf{u}_R, & \text{if } \frac{x}{t} \geq S_R \end{cases} \quad (14)$$

where the \mathbf{u}_L^* and \mathbf{u}_R^* can be calculated using relationships derived from the Rankine-Hugoniot conditions

$$\mathbf{F}_L^* = \mathbf{F}_L + S_L (\mathbf{u}_L^* - \mathbf{u}_L) \quad (15)$$

$$\mathbf{F}_R^* = \mathbf{F}_R + S_R (\mathbf{u}_R^* - \mathbf{u}_R). \quad (16)$$

4.2. Wave Speed Estimate for MHD

In order to use the approximate Riemann solvers, bound estimates for the two fastest wave speeds emerging from the solution of Riemann problem needs to be provided.[21] For solving MHD system, maximum and minimum wave speeds S_L and S_R can be taken as

$$S_L = \min(v_{x,L}, v_{x,R}) - \max(c_{f,L}, c_{f,R}) \quad (17)$$

$$S_R = \max(v_{x,L}, v_{x,R}) + \max(c_{f,L}, c_{f,R}) \quad (18)$$

By making the assumption that the intermediate wave between \mathbf{u}_L^* and \mathbf{u}_R^* is a contact discontinuity moving at speed $S^* = v_{x,L}^* = v_{x,R}^*$, S^* can be written as

$$S^* = \frac{p_R - p_L + \Delta \rho u + B_{x,L}^2 - B_{x,R}^2}{\rho_L (S_L - u_L) - \rho_R (S_R - u_R)} \quad (19)$$

where $\Delta \rho u = \rho_L u_L (S_L - u_L) - \rho_R u_R (S_R - u_R)$.

4.3. HLLC Solver for MHD

Using the consistency condition, it can be shown that solving MHD system with the conventional HLLC solver presented in section 4.1 gives solution which is inconsistent with the integral form of the MHD equations.

$$\frac{v_x^* - S_L}{S_R - S_L} \mathbf{u}_L^* + \frac{S_R - v_x^*}{S_R - S_L} \mathbf{u}_R^* = \frac{S_R \mathbf{u}_R - S_L \mathbf{u}_L - (\mathbf{f}_R - \mathbf{f}_L)}{S_R - S_L} = \mathbf{u}^{HLL} \quad (20)$$

Li[12] has proposed a modified MHD-HLLC scheme which retains most of the standard HLLC properties.

$$p_T^* = \rho (S_K - v_{x,K}) (v_x^* - v_{x,K}) + p + \frac{1}{2} B^2 - B_{x,K}^2 + (B_{x,K}^*)^2 \quad (21)$$

$$\rho_K^* = \rho_K \frac{S_K - v_{x,K}}{S_K - v_x^*} \quad (22)$$

$$(\rho v_x)^*_K = \rho_K^* v_x^* \quad (23)$$

$$(\rho v_{(y,z)})_K^* = \rho_K v_{(y,z),K} \frac{S_K - v_{x,K}}{S_K - v_x^*} - \frac{B_{x,K}^* B_{(y,z),K}^* - B_{x,K} B_{(y,z),K}}{S_K - v_x^*} \quad (24)$$

$$U_K^* = U_K \frac{S_K - v_{x,K}}{S_K - v_x^*} + \frac{p_T^* v_x^* - p_{T,K} v_{x,K} - [B_x^* (\mathbf{B} \cdot \mathbf{v})^* - B_{x,K} (\mathbf{B} \cdot \mathbf{v})]}{S_L - v_{x,K}} \quad (25)$$

Here $K \in \{L, R\}$ depending on the side of Riemann problem to be solved. The equations (21) - (25) derived from Rankine Hugoniot condition can still be used with slight modifications. In order to resolve the issue with consistency, the intermediate magnetic field components need to be replaced by the respective HLL intermediate state, hence $B_x^* = B_x^{HLL}$, $B_y^* = B_y^{HLL}$ and $B_z^* = B_z^{HLL}$. Additionally, $(\mathbf{B} \cdot \mathbf{v})^*$ in the energy equation needs to be replaced by $(\mathbf{B}^{HLL} \cdot \mathbf{v}^{HLL})$ for the equation to satisfy the consistency condition.

4.4. FORCE Solver for MHD

The First Order Centred (FORCE) scheme can also be used to solve the ideal MHD equations by replacing the Godunov upwind flux with FORCE flux. FORCE flux can be obtained by taking the average between Lax-Friedrichs and Richtmyer Fluxes

$$\mathbf{f}_{i+\frac{1}{2}}^{\text{FORCE}} = \frac{1}{2} \left[\mathbf{f}_{i+\frac{1}{2}}^{\text{LF}}(\mathbf{u}_L, \mathbf{u}_R) + \mathbf{f}_{i+\frac{1}{2}}^{\text{RI}}(\mathbf{u}_L, \mathbf{u}_R) \right] \quad (26)$$

where the Lax-Friedrichs flux can be obtained by

$$\mathbf{f}_{i+\frac{1}{2}}^{\text{LF}} = \frac{1}{2} [\mathbf{f}(\mathbf{u}_L) + \mathbf{f}(\mathbf{u}_R)] + \frac{1}{2} \frac{\Delta x}{\Delta t} [\mathbf{u}_L - \mathbf{u}_R] \quad (27)$$

and the second-order accurate Richtmyer flux from

$$\mathbf{u}_{i+\frac{1}{2}}^{\text{RI}} = \frac{1}{2} (\mathbf{u}_L + \mathbf{u}_R) + \frac{1}{2} \frac{\Delta t}{\Delta x} [\mathbf{f}(\mathbf{u}_L) - \mathbf{f}(\mathbf{u}_R)] \quad (28)$$

$$\mathbf{f}_{i+\frac{1}{2}}^{\text{RI}} = \mathbf{f}(\mathbf{u}_{i+\frac{1}{2}}^{\text{RI}}). \quad (29)$$

4.5. Dimensional Splitting

Dimensional splitting approach has been adopted in this paper to solve the multidimensional Euler system numerically. In this approach, 1-D method is being applied in each coordinate direction, starting with the x-direction update followed by y-direction update.[21]

$$\begin{aligned} \bar{\mathbf{u}}_{i,j} &= \mathbf{u}_{i,j}^n + \frac{\Delta t}{\Delta x} (\mathbf{f}_{i-1/2,j}^n(\mathbf{u}) - \mathbf{f}_{i+1/2,j}^n(\mathbf{u})) \\ \mathbf{u}_{i,j}^{n+1} &= \bar{\mathbf{u}}_{i,j} + \frac{\Delta t}{\Delta y} (\mathbf{g}_{i,j-1/2}^n(\bar{\mathbf{u}}) - \mathbf{g}_{i,j+1/2}^n(\bar{\mathbf{u}})) \end{aligned} \quad (30)$$

This method allows diagonal movement of information and the standard CFL number can be used without any reduction. In addition, the solution can be extended to second order accurate in space and time using Strang splitting method.[15]

$$\mathbf{u}_{i,j}^{n+1} = \frac{1}{2} \left[\mathcal{Y}^{(\Delta t)} \mathcal{X}^{(\Delta t)} + \mathcal{X}^{(\Delta t)} \mathcal{Y}^{(\Delta t)} \right] (\mathbf{u}^n) \quad (31)$$

Note that in this paper Strang splitting was not implemented.

4.6. Second order extension

The Monotone Upstream-centred Scheme for Conservation Laws (MUSCL) approach allows the construction of higher order schemes by modifying the piece-wise constant data. In order to maintain the monotonicity of the scheme, the reconstruction is constrained so the spurious oscillation can be avoided. [21]

4.6.1. Data Reconstruction

The first step for constructing a second order extension flux $\mathbf{f}_{i+0.5}$ is to replace the cell averaged values by reconstructed boundary values using derivative approximation.

$$\mathbf{u}_i^L = \mathbf{u}_i^n - \frac{1}{2} \Delta_i; \quad \mathbf{u}_i^R = \mathbf{u}_i^n + \frac{1}{2} \Delta_i \quad (32)$$

Given that the derivatives do not exist at discontinuities, spurious oscillations can be generated in regions of strong gradients. This aligns with the Godunov's Theorem which states that the desirable properties of accuracy and monotonicity are contradictory requirements.[21] In order to construct a second order Total Variation Diminishing (TVD) scheme, the slopes Δ_i in the reconstruction steps can be replaced by limited slopes $\bar{\Delta}_i = \xi_i \Delta_i$, according to some TVD constraints. The reconstruction will be fully limited to piece-wise constant in cases of high change in slope while no limiting will be applied in cases of smooth change in slope. In this paper, MINBEE-type and VAN LEER-type slope limiters have been used to limit the slopes. A VAN LEER-type slope limiter is

$$\xi_{VL}(r) = \begin{cases} 0, & \text{if } r \leq 0 \\ 2r, & \text{if } 0 \leq r \leq \frac{1}{2} \\ 1, & \text{if } \frac{1}{2} \leq r \leq 1 \\ \min\{r, \xi_R(r), 2\}, & \text{if } r \geq 1 \end{cases} \quad (33)$$

A MINBEE-type slope limiter is

$$\xi_{MB}(r) = \begin{cases} 0, & r \leq 0 \\ r, & 0 \leq r \leq 1 \\ \min\{1, \xi_R(r)\}, & r \geq 1 \end{cases} \quad (34)$$

where $r = \frac{\Delta_{i-1/2}}{\Delta_{i+1/2}}$ and $\xi_R(r) = \frac{2}{1+r}$.

4.6.2. MUSCL Hancock scheme

Within each cell, the boundary extrapolated values are evolved locally at half time step as

$$\begin{aligned}\bar{\mathbf{u}}_i^L &= \mathbf{u}_i^L + \frac{1}{2} \frac{\Delta t}{\Delta x} [\mathbf{f}(\mathbf{u}_i^L) - \mathbf{f}(\mathbf{u}_i^R)] \\ \bar{\mathbf{u}}_i^R &= \mathbf{u}_i^R + \frac{1}{2} \frac{\Delta t}{\Delta x} [\mathbf{f}(\mathbf{u}_i^L) - \mathbf{f}(\mathbf{u}_i^R)]\end{aligned}\quad (35)$$

The evolved boundary values $\bar{\mathbf{u}}_{i+1}^L$ and $\bar{\mathbf{u}}_i^R$ are then being treated as the initial values for HLL and HLLC Riemann Solver to produce second order accurate numerical simulation. Once the intercell fluxes have been computed, Godunov's method can be used as a means to update the data.

4.6.3. SLIC scheme

The Slope Limiter Centred (SLIC) Scheme is a second order extension of the FORCE scheme. This scheme uses the same method to construct the boundary extrapolated values and perform local evolution as described in section 4.6.1 and section 4.6.2 respectively. FORCE flux can be evaluated by

$$\mathbf{f}_{i+\frac{1}{2}}^{\text{SLIC}} = \mathbf{f}_{i+\frac{1}{2}}^{\text{FORCE}}(\bar{\mathbf{u}}_i^R, \bar{\mathbf{u}}_{i+1}^L) \quad (36)$$

and being used in equation (9) for conservative update.

4.7. Divergence Cleaning

In order to enforce the constraint $\nabla \cdot \mathbf{B} = 0$, Dedner et al.[5] has proposed a hyperbolic divergence cleaning method which works by adding a generalised Lagrangian multiplier (GLM) ψ to equation (1d) and (1e),

$$\frac{\partial \mathbf{B}}{\partial t} + \nabla \cdot (\mathbf{B} \otimes \mathbf{v} - \mathbf{v} \otimes \mathbf{B}) + \nabla \psi = 0 \quad (37)$$

$$\mathcal{D}(\psi) + \nabla \cdot \mathbf{B} = 0 \quad (38)$$

where $\mathcal{D}(\cdot)$ is a linear differential operator. This system is called the GLM formulation of MHD equations (GLM-MHD). GLM-MHD reduces the divergence errors by damping the errors while transporting them to the domain boundaries with the maximum possible speed.

4.7.1. Parabolic Correction

The linear differential operator can be defined as

$$\mathcal{D}(\psi) = \frac{1}{c_p^2} \psi \quad (39)$$

where $c_p \in \{0, \infty\}$. Although this correction can smooth out the perturbations in magnetic field, the restrictions being imposed on c_p due to stability conditions from explicit solvers can lead to certain difficulties.

4.7.2. Hyperbolic Correction

To perform hyperbolic correction, the linear differential operator can be defined as

$$\mathcal{D}(\psi) = \frac{1}{c_h^2} \partial_t \psi \quad (40)$$

where $c_h \in \{0, \infty\}$. The main advantage of using hyperbolic correction is the result of a consistent hyperbolic system even after coupling the divergence constraint to the evolution equations. This method allows the local divergence error to be transported to the boundary with finite speed c_h .

4.7.3. Mixed Correction

Combining the parabolic and hyperbolic corrections, the linear differential operator can be defined as

$$\mathcal{D}(\psi) = \frac{1}{c_h^2} \partial_t \psi + \frac{1}{c_p^2} \psi. \quad (41)$$

This method allows the divergence errors to be transported with speed c_h and damped with time and distance. As with the other correction methods, equation (38) can then be written in the following format which introduces an additional hyperbolic equation to solve

$$\partial_t \psi + c_h^2 (\nabla \cdot \mathbf{B}) = -\frac{c_p^2}{c_h^2} \psi \quad (42)$$

Dedner *et al.* [5] has recommended the value of $\frac{c_p^2}{c_h}$ to be 0.18.

4.7.4. Implementation

The GLM-MHD system with mixed correction is proven to be hyperbolic with an in-homogeneous part containing a source term in the evolution equation for ψ . Additionally, while writing the system in primitive variable form, it can be observed that the equations for B_x and ψ decouple from the remaining system hence can be solved independently.

$$\partial_t \begin{pmatrix} B_x \\ \psi \end{pmatrix} + \begin{pmatrix} 0 & 1 \\ c_h^2 & 0 \end{pmatrix} \partial_x \begin{pmatrix} B_x \\ \psi \end{pmatrix} = \begin{pmatrix} 0 \\ 0 \end{pmatrix} \quad (43)$$

In order to solve the GLM-MHD system using the Godunov approach, numerical flux for the hyperbolic GLM-MHD with no source terms needs to be defined. The numerical flux for $(\tilde{\psi}, \tilde{B}_x)$ can be written in the form of

$$\begin{pmatrix} \tilde{B}_x \\ \tilde{\psi} \end{pmatrix} = \begin{pmatrix} \frac{1}{2} (B_{x,L} + B_{x,R}) - \frac{1}{2c_h} (\psi_R - \psi_L) \\ \frac{1}{2} (\psi_L + \psi_R) - \frac{c_h}{2} (B_{x,R} - B_{x,L}) \end{pmatrix} \quad (44)$$

for arbitrary left and right states $(B_{x,L}, \psi_L)$ and $(B_{x,R}, \psi_R)$. For the rest of the system, seven wave Riemann solver can be used for the 1-D MHD equations with the normal component of the magnetic field replaced by \tilde{B}_x . The source term on the evolution equation for ψ can be solved using an operator splitting approach. In this paper, first order accurate Euler method has been used with the recommended initial value of 0 for ψ . [10]

$$\mathbf{u}^{n+1} = \mathbf{u}^n + \Delta t \mathbf{s}(\mathbf{u}^n) \quad (45)$$

Furthermore, the boundary condition for ψ was set to be having identical behaviour as the rest of the variables as recommended by Dedner *et al.* [5]

5. Test Results

In this section, test results for 1-D and 2-D MHD problems will be presented. The initial data for the problems are defined in primitive variable.

$$\mathbf{w} = (\rho, v_x, v_y, v_z, B_x, B_y, B_z, P)^T \quad (46)$$

5.1. 1-D Sod test

The MHD code was first tested with the Sod test to ensure the code is working for the Euler equations. The test has

been simulated at several grid resolutions of $N=100, 200, 400$ across the simulation domain of $x \in \{0, 1\}$ with the initial discontinuity at $x = 0.5$. The initial condition for this test problem is as follow

$$\begin{aligned} \mathbf{w}_L &= (1, 0, 0, 0, 1, 0, 0, 0)^T \\ \mathbf{w}_R &= (0.125, 0, 0, 0, 0.1, 0, 0, 0)^T \end{aligned} \quad (47)$$

where $\mathbf{B} = 0$ everywhere in the domain. Transmissive boundary condition and Cfl number of 0.9 have been applied to all the test cases. The plots for density, velocity, pressure and specific internal energy have been produced for all the test cases. The exact solution for all the test cases have been computed using the exact Riemann Solver and included in the plots. As shown in the results (Figure 1a-2b), the solution consists of a left rarefaction, a contact and a right shock.

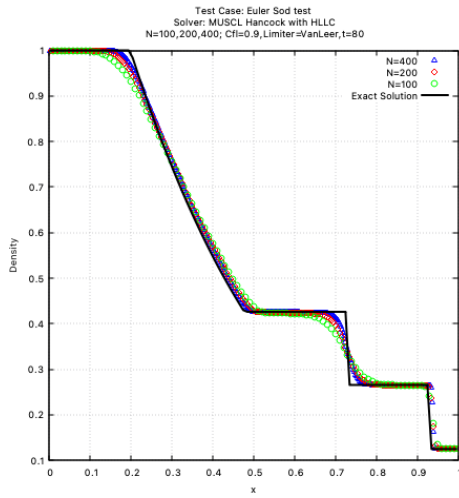
5.2. Brio and Wu test

The first numerical example with non zero magnetic field is a coplanar MHD Riemann problem with initial data consisting of two constant states. Note that the initial hydrodynamical data for this test case are identical to the Sod test. For this test case, simulation has been carried out across the domain of $x \in \{0, 800\}$ with the initial discontinuity at $x = 400$. The simulation end time for this test case is 80s and gamma is being set to 2. Transmissive boundary has been applied to this test case together with Cfl number of 0.8.

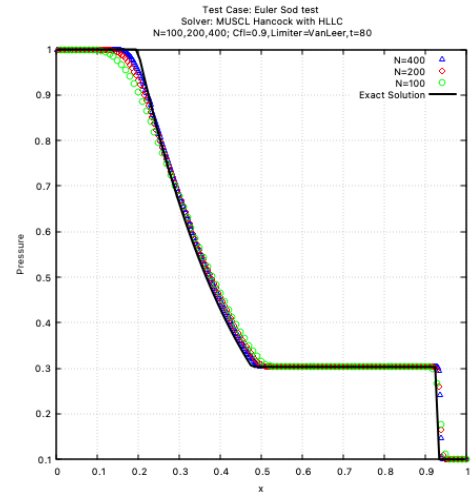
$$\begin{aligned} x \leq 400 \quad \mathbf{w}_L &= (1, 0, 0, 0, 1, 0.75, 1, 0)^T \\ x > 400 \quad \mathbf{w}_R &= (0.125, 0, 0, 0, 0.1, 0.75, -1, 0)^T \end{aligned} \quad (48)$$

The results for this 1-D test case at different resolutions ($N=100, 200, 400, 800$) are shown in Figure (3a-4b). Given the complexity of implementing an exact Riemann solver for 1-D MHD, simulation result produced at $N=8000$ is being treated as the exact solution to the test case. Referring to the density plot (Figure 3a), moving to the left from contact discontinuity, C, there are compound wave, CM and fast rarefaction wave, FR. The contact discontinuity is moving to the right together with a slow shock, SS and fast rarefaction wave, FR. Compound wave is made up of a shock and rarefaction wave of the same family. The compound wave exists due to the non-convexity of the MHD equations.[2]

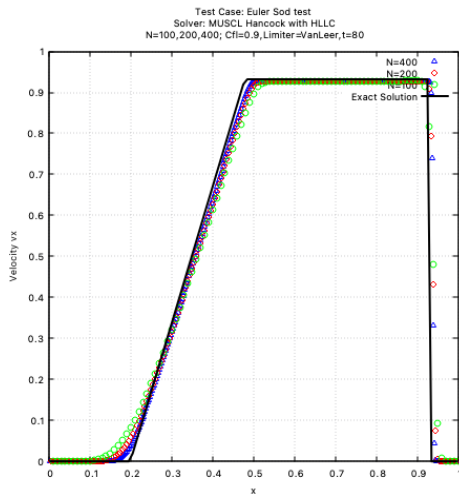
1-D Sod test results



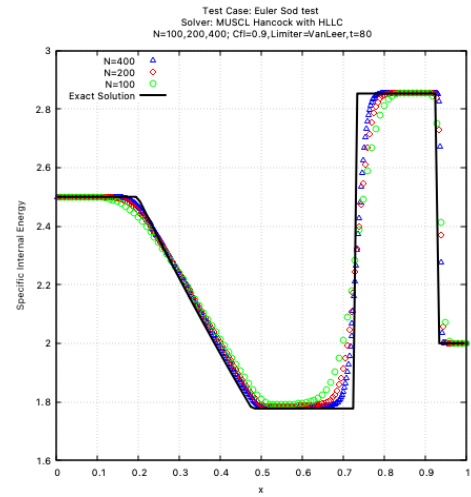
(a) Density plot



(a) Pressure plot



(b) Velocity vx plot

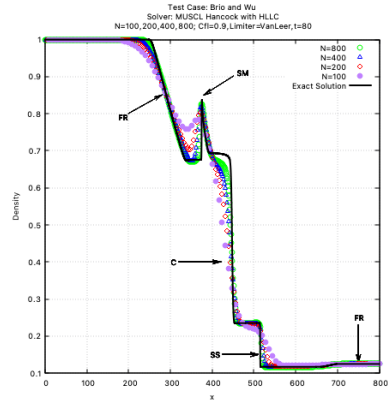


(b) Specific Internal Energy plot

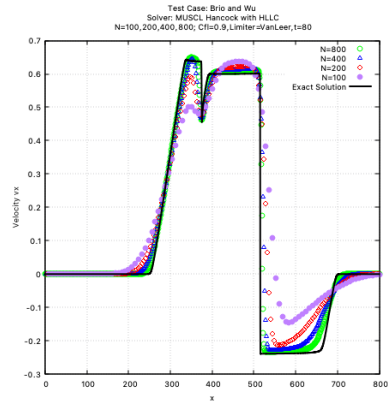
Figure 1: Density and velocity vx plots from 1-D Sod test at N=100, 200, 400

Figure 2: Pressure and specific internal energy plots from 1-D Sod test at N=100, 200, 400

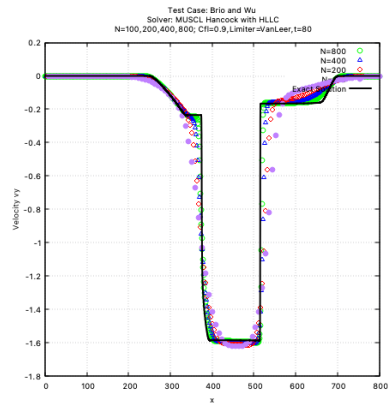
1-D Brio and Wu test results



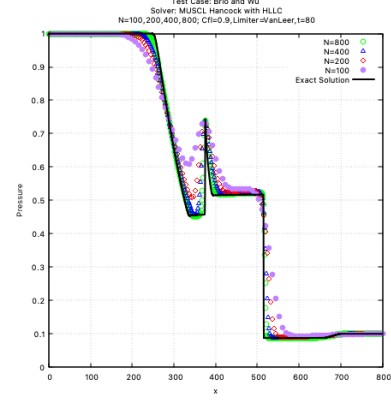
(a) Density plot



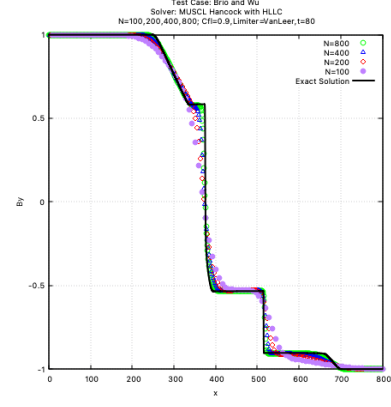
(b) Velocity vx plot



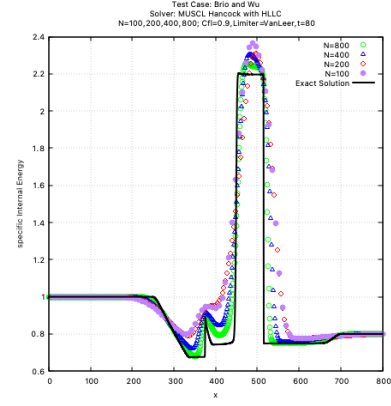
(c) Velocity y plot



(a) Pressure plot



(b) Magnetic field y plot



(c) Specific Internal Energy plot

Figure 3: Density, velocity vx and vy from Brio and Wu test at N=100, 200, 400, 800

Figure 4: Pressure, By and Specific Internal Energy plots from Brio and Wu test at N=100, 200, 400, 800

5.3. 2-D Sod test

The 2-D MHD code is first tested with the Sod test at a resolution of $N = 200 \times 200$. Two versions of the test have been carried out; first one where the initial contact discontinuity exists at $x=0.5$, and second one where the initial contact discontinuity exists at $y=0.5$. 1-D plots taken along $y=0.5$ for the first version and $x=0.5$ for the second version have been produced at Figure (7a-8d). As shown in the test results, the two versions give identical results when being considered in the appropriate dimension.

The Sod test is then repeated with the contact discontinuity being represented by the line $y = 1 - x$. 1-D plots taken along $y=x$ have been produced at Figure (9a-9d). The results are similar to the original Sod test except at the regions near the boundary. When transmissive boundary condition is being applied, the ghost cells' values are constantly extrapolated from both ends of the simulation domain. In the case of diagonally aligned Sod test, the flow is diagonal as opposed to orthogonal in the original test hence extra wave interactions have been observed near the boundaries. Note that the colour plots for these test cases are included in Appendix A.

5.4. Cylindrical Explosion test

For this test case, the 2-D Euler equations are being solved on a square domain of $x \in \{0, 2\}, y \in \{0, 2\}$. The initial condition is made up of a region inside a circle of radius $R=0.4$ centred at $(1,1)$ and the region outside the circle. Transmissive boundary condition has been applied and the limiter function used at the slope reconstruction step is Van-Leer. The values of the initial condition are as follow

$$\begin{aligned} \rho_{ins} &= 1.0, & \rho_{out} &= 0.125, \\ u_{ins} &= 0.0, & u_{out} &= 0.0, \\ v_{ins} &= 0.0, & v_{out} &= 0.0, \\ p_{ins} &= 1.0, & p_{out} &= 0.1. \end{aligned} \quad (49)$$

where subscripts *ins* and *out* represent inside and outside the circle respectively.

2-D density and pressure plots have been produced at the output time $t=0.25$ and presented in Figure (5-6). The density plot shows the circular shock travelling outwards

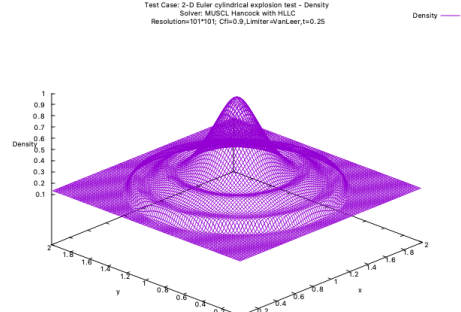


Figure 5: Density plot from cylindrical explosion test

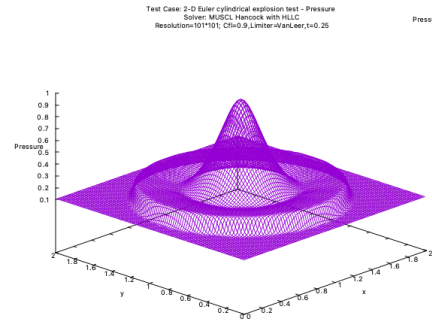
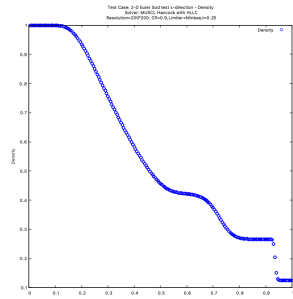


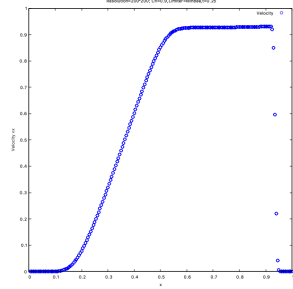
Figure 6: Pressure plot from cylindrical explosion test

from centre together with the contact surface and a circular rarefaction travelling towards the centre. As shown in the pressure plot, pressure is continuous across the contact surface. In addition, 1-D plots have been produced at the midpoint for y -direction and shown in Figure (10a-10d). Comparing these 1-D plots with Figure 17.4 in Toro's book, the results here match all the characteristics shown in the exact solution. Note that for this paper, initial data within the quadrilateral cells cutting the initial discontinuity are not being modified. This explains the small amplitude waves observed near the contact discontinuity formed at early times by the staircase configuration of initial data. This can be resolved by assigning modified area-weighted values to the appropriate cells at initial time and has been identified as a future improvement.[21]

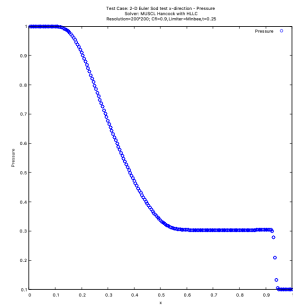
2-D Sod test with x-split and y-split IC results



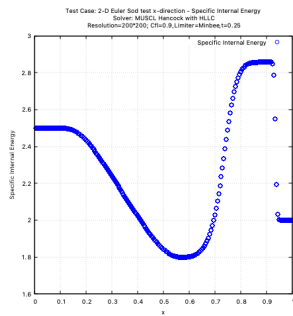
(a) Density plot



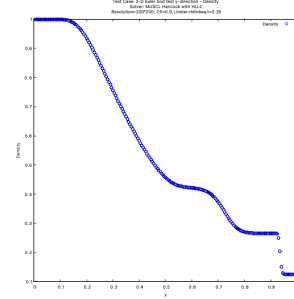
(b) Velocity vx plot



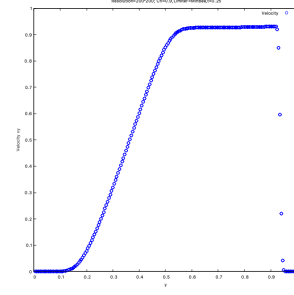
(c) Pressure plot



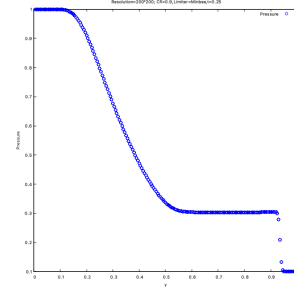
(d) Specific Internal Energy plot



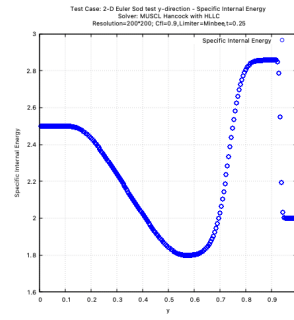
(a) Density plot



(b) Velocity vy plot



(c) Pressure plot

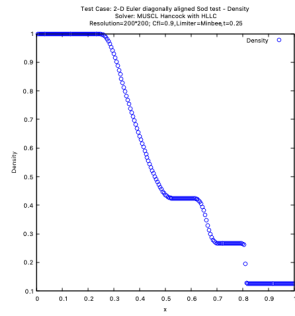


(d) Specific Internal Energy plot

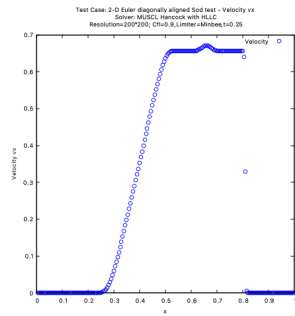
Figure 7: Plots at $y=0.5$ from 2-D Sod test x-split

Figure 8: Plots at $x=0.5$ from 2-D Sod test y-split

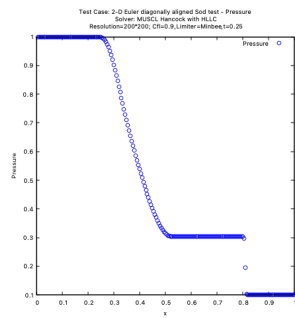
2-D diagonally aligned Sod test results



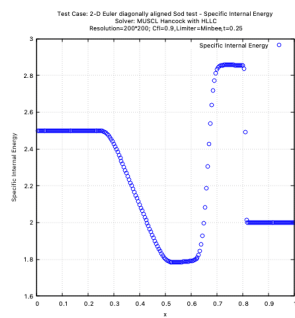
(a) Density plot



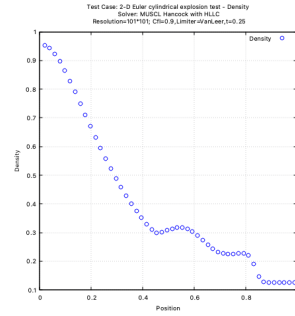
(b) Velocity vx plot



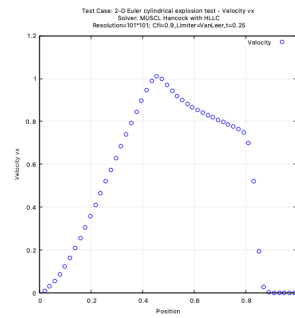
(c) Pressure plot



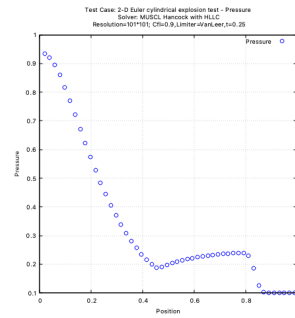
(d) Specific Internal Energy plot



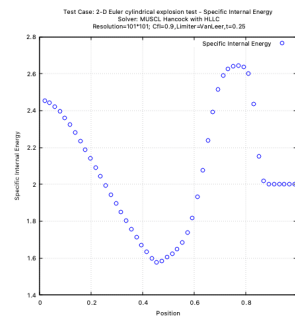
(a) Density plot



(b) Velocity vx plot



(c) Pressure plot



(d) Specific Internal Energy plot

Figure 9: Plots at $x=y$ from 2-D diagonally aligned Sod test

Figure 10: 1-D slice plots from cylindrical explosion test

5.5. 2-D Brio and Wu test

The Brio and Wu test in Section 5.2 is repeated at a resolution of $N=800 \times 800$ across a square domain of $x \in \{0, 800\}, y \in \{0, 800\}$. Two versions of the test have been carried out; first one where the initial contact discontinuity exists at $x=400$, and second one where the initial contact discontinuity exists at $y=400$. 1-D plots taken along $y=400$ for the first version and $x=400$ for the second version have been produced at Figure (11-21). As shown in the test results, the two versions give identical results when being considered in the appropriate dimension. Note that the colour plots for these test cases are included in Appendix B.

5.6. Orszag-Tang vortex test

Orszag-Tang vortex is a common test for 2-D numerical MHD codes. Starting from a smooth initial field configuration, the vortex quickly forms shocks before transitioning to 2D MHD turbulence. The problem testing the robustness of the code at handling the formation of MHD shocks, and shock-shock interactions. Additionally, the problem is capable of providing some estimates of the impact of magnetic monopoles on the numerical simulations, testing the $\nabla \cdot \mathbf{B} = 0$ limit.[1] The initial conditions for the test are

$$w = \begin{bmatrix} \gamma^2 \\ -\sin(2\pi y) \\ \sin(2\pi x) \\ 0 \\ -\sin(2\pi y) \\ \sin(4\pi x) \\ 0 \\ \gamma \end{bmatrix}. \quad (50)$$

The initial velocities are periodic while the magnetic field is initialized using a periodic vector potential defined at zone corners.[1] The boundary conditions are periodic everywhere for this test case and a square domain of $0 \leq x \leq 1; 0 \leq y \leq 1$ is used in the simulation. MINBEE limiter has been chosen as the slope limiter as it is known to maintain a positive solution in multiple space dimension.[10] Density distribution at times $t = 0.5$ and $t = 1.0$ are shown in Figure 23a and 23b. The results

show some formation of small scale vortices and turbulence. Hyperbolic divergence cleaning as described in Section 4.7 has been applied to these test cases and the density distributions are presented in Figure 24a and 24b.

5.7. Kelvin-Helmholtz instability test

Kelvin Helmholtz (KH) instability can be observed at the boundary layer of two fluids in relative motion. The introduction of magnetic field to a simple conducting shear flow is expected to introduce several effects which may change the evolution of the stability significantly. The initial condition for the test case are

$$w = \begin{bmatrix} 1.0 \\ M/2(\tanh(20y)) \\ 0.1 \sin(2\pi x) (e^{-y^2/\sigma^2}) \\ 0.0 \\ c_a \sqrt{\rho} \cos(\theta) \\ 0.0 \\ c_a \sqrt{\rho} \sin \\ 1/\gamma \end{bmatrix} \quad (51)$$

where $\theta = \pi/3, M = 1, c_a = 0.1, \sigma = 0.1$. The boundary conditions for this test case are reflective across the y-direction and periodic across the x-direction. The simulation domain for this test case is $0 \leq x \leq 1; -1 \leq y \leq 1$ and MINBEE has been chosen as the slope limiter for this test. Plots at time = 5s, 8s, 12s, 20s showing the ratio of the poloidal field strength and the toroidal component are presented in Figure 25. Hyperbolic divergence cleaning as described in Section 4.7 has been applied to these test cases and the density distributions are presented in Figure 26.

At early times of the simulation ($t=5s$ and $8s$), the magnetic field is strongly amplified by the vortical motions developed from the unstable modes growth and become locally dominant. The vortical motions can then act as a mediator for energy transfer to small scales, at which it can be dissipated by localised reconnection event. When the instability is active, shear layer decays into an enlarged, steady vortex sheet which the magnetic field revert back to its original state while the flow material has been completely mixed. At the end of the simulation, the width of the final layer is bigger than it was initially, roughly equal to the size of initial perturbation.[14]

2-D Brio and Wu with x-split IC test results

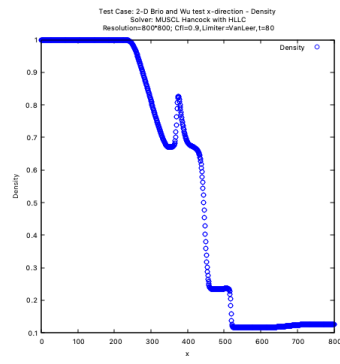


Figure 11: Density plot at $y=400$ from 2-D Brio and Wu test

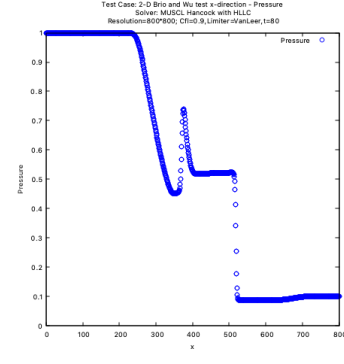


Figure 14: Pressure plot at $y=400$ from 2-D Brio and Wu test

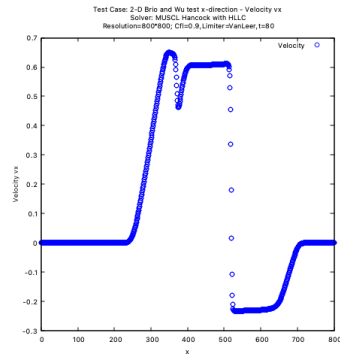


Figure 12: Velocity v_x plot at $y=400$ from 2-D Brio and Wu test

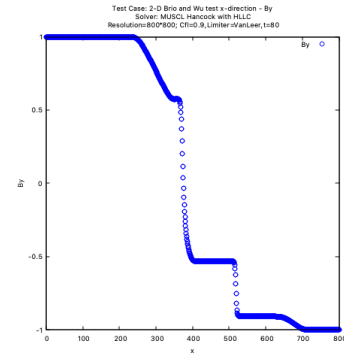


Figure 15: B_y plot at $y=400$ from 2-D Brio and Wu test

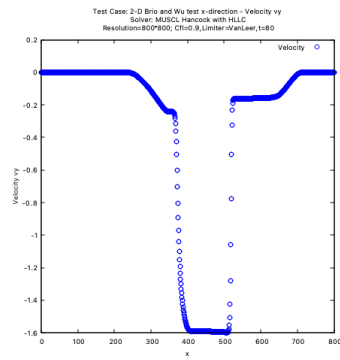


Figure 13: Velocity v_y plot at $y=400$ from 2-D Brio and Wu test

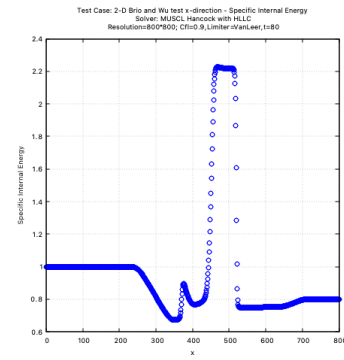


Figure 16: Specific Internal Energy plot at $y=400$ from 2-D Brio and Wu test

2-D Brio and Wu with y-split IC test results

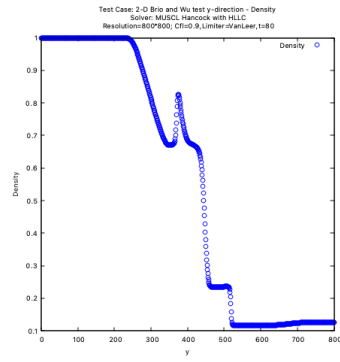


Figure 17: Density plot at $x=400$ from 2-D Brio and Wu test

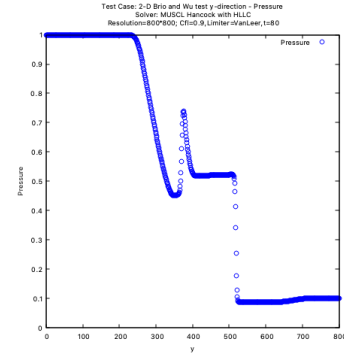


Figure 20: Pressure plot at $x=400$ from 2-D Brio and Wu test

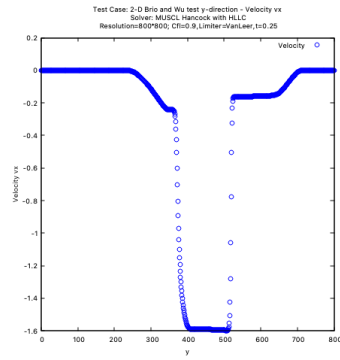


Figure 18: Velocity v_x plot at $x=400$ from 2-D Brio and Wu test

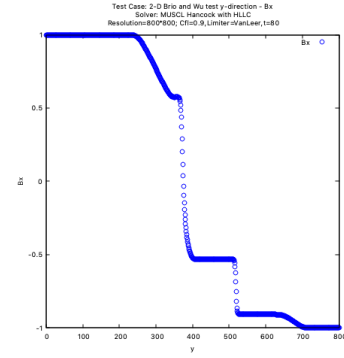


Figure 21: B_x plot at $x=400$ from 2-D Brio and Wu test

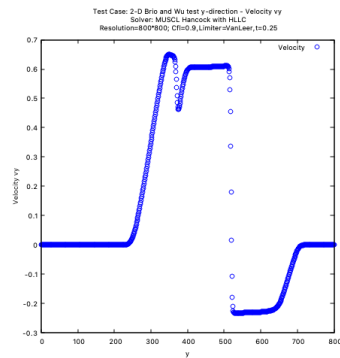


Figure 19: Velocity v_y plot at $x=400$ from 2-D Brio and Wu test

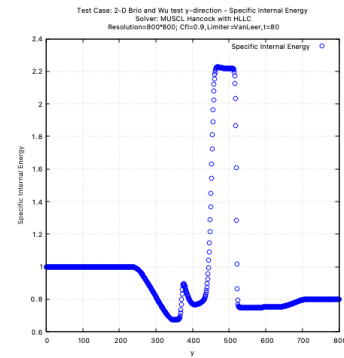
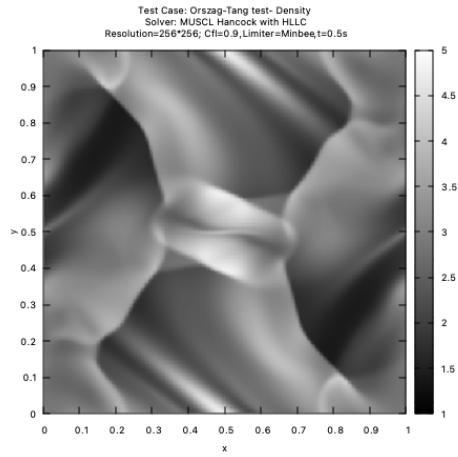
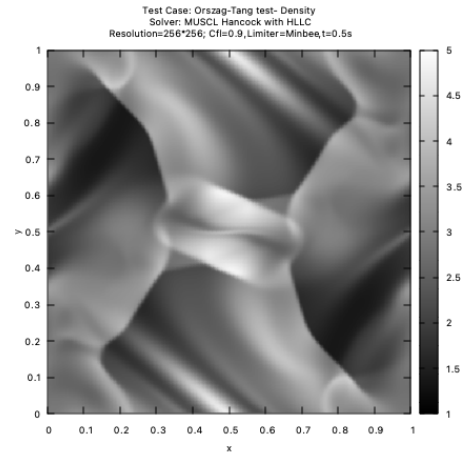


Figure 22: Specific Internal Energy plot at $x=400$ from 2-D Brio and Wu test

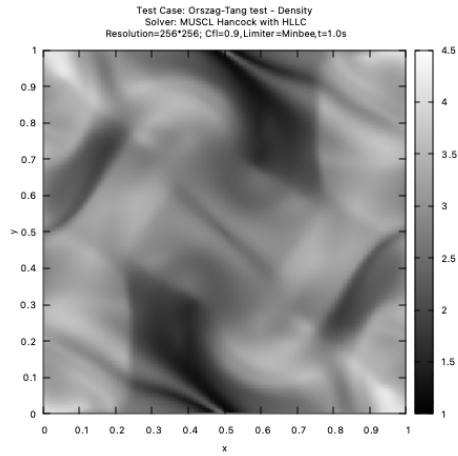
Orszag-Tang test results



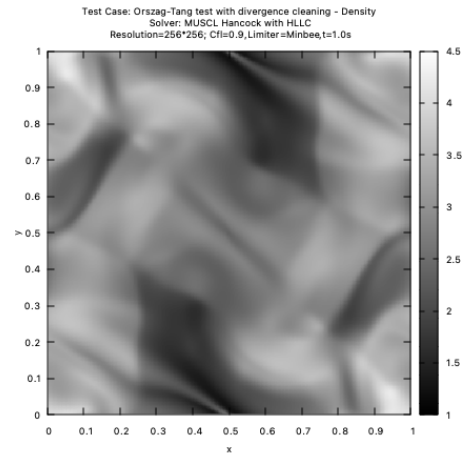
(a) $t=0.5s$



(a) $t=0.5s$ with divergence cleaning



(b) $t=1.0s$



(b) $t=1.0s$ with divergence cleaning

Figure 23: Density plots for Orszag-Tang test at 0.5s and 1s

Figure 24: Density plots for Orszag-Tang test at 0.5s and 1s with hyperbolic divergence cleaning

Kelvin-Helmholtz test results

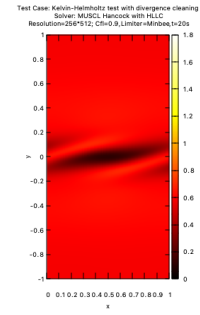
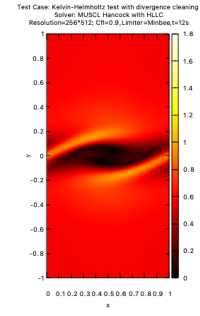
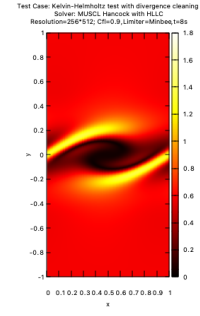
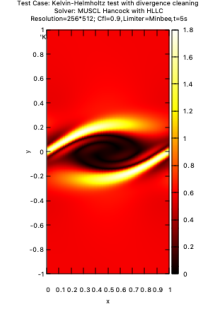
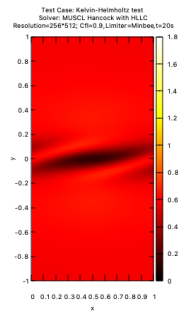
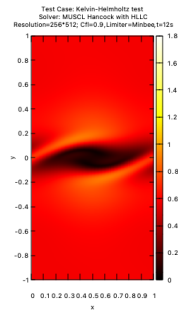
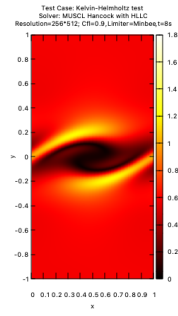
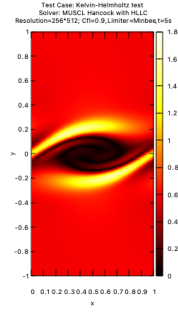


Figure 25: $\sqrt{B_x^2 + B_y^2}/B_z$ plots for Kelvin-Helmholtz test at $t=5s, 8s, 12s, 20s$ (top to bottom)

Figure 26: $\sqrt{B_x^2 + B_y^2}/B_z$ plots for Kelvin-Helmholtz test with hyperbolic divergence cleaning at $t=5s, 8s, 12s, 20s$ (top to bottom)

6. Discussion

Convergence analysis has been performed on the simulation results of Brio and Wu 1-D test with MUSCL-Hancock scheme. As shown in Table 1, the L_p - norms decreases as the resolution improves with increasing mesh. This validates the theory of increasing accuracy with the resolution. Furthermore, the convergence analysis is repeated for the Brio and Wu 1-D test with SLIC scheme. As shown in Table 2, similar trend of decreasing L_p - norms as the resolution improves has been observed. However, the L_p - norms for using SLIC scheme are generally greater than the L_p - norms from the simulations using MUSCL Hancock scheme. This shows that the Godunov's method is better at capturing discontinuity and provides more accurate numerical approximation.

The L_1 - norm of the divergence $\nabla \cdot \mathbf{B}$ can be computed by taking the central difference between cells. Figure 28 and 29 show the $L_1(\nabla \cdot \mathbf{B})$ throughout the simulation time for Orszag-Tang and Kelvin-Helmholtz test respectively. It can be observed from these plots that the $L_1(\nabla \cdot \mathbf{B})$ for the case of using hyperbolic divergence cleaning seem to converge to zero as time increases. This shows that the mixed GLM approach is working as expected.

Mesh	Δx	L_1	L_2	L_∞
100	8.0	0.0310406	0.067608	0.354156
200	4.0	0.0194917	0.0488199	0.301111
400	2.0	0.0118913	0.0340702	0.243677
800	1.0	0.00691243	0.0226477	0.182095

Table 1: L_p -norms for Brio & Wu test using MUSCL-Hancock scheme.

Mesh	Δx	L_1	L_2	L_∞
100	8.0	0.0592036	0.0851648	0.253153
200	4.0	0.039961	0.0701155	0.277158
400	2.0	0.0269997	0.0559079	0.267186
800	1.0	0.0135897	0.036174	0.220055

Table 2: L_p -norms for Brio & Wu test using SLIC scheme.

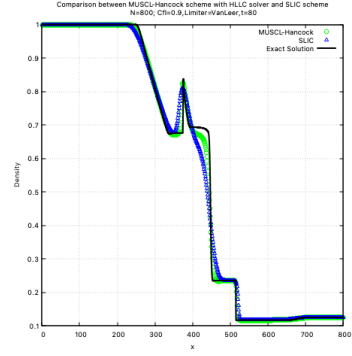


Figure 27: Comparison between MUSCL-Hancock and SLIC scheme

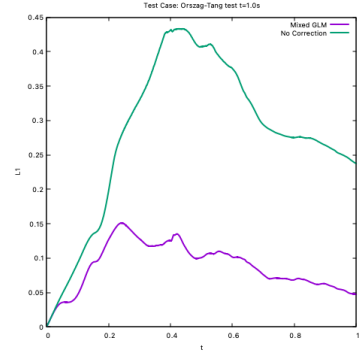


Figure 28: $L_1(\nabla \cdot \mathbf{B})$ for Orszag-Tang test at $t=1.0s$

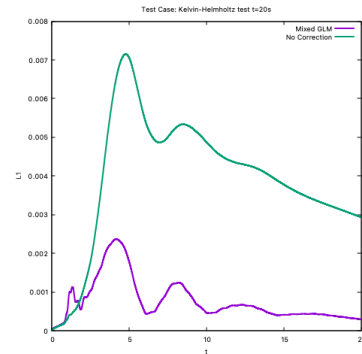


Figure 29: $L_1(\nabla \cdot \mathbf{B})$ for Kelvin-Helmholtz test at $t=20s$

7. Conclusions

In this paper, 1-D and 2-D ideal MHD systems are being solved using the modified HLLC solver proposed by Li[12]. In order to maintain a divergence free simulation, hyperbolic divergence cleaning proposed by Dedner et al.[5] has been implemented on the orszag-Tang and Kelvin Helmholtz test cases. As demonstrated in Figure 28 and 29, the divergence cleaning is successful in enforcing $\nabla \cdot \mathbf{B}$ simulation.

One of the obvious advantages of adopting the hyperbolic cleaning method is due to the ease of implementation given that it is based on the cell-centered discretisations favored in Godunov scheme.[10] The extension of divergence cleaning method to higher order finite volume schemes is straightforward.[5] However, the downside of this approach is the dependency on tunable parameters $\frac{c_p^2}{c_h}$. In the future, the implementation of constrained transport approach which relies on a staggered formulation of magnetic and electric fields should be explored. Although this approach can be more complex, the method is advantageous as the magnetic field will be inherently divergence free.

In addition, simulation of resistive MHD should be performed in the future given that for most terrestrial applications such as fusion reactor simulations, lightning and many other astrophysical ones, cannot neglect resistivity. In addition, simulations involving complicated mixtures such as plasma and air can be carried out using tabulated equation of state.

Finally, Adaptive Mesh Refinement (AMR) can be adopted to refine the solution of MHD to display the sharp features at higher resolutions. Parallel computing using MPI and OpenMP can also be leveraged to improve the simulation time of MHD system.

Appendix A. Colour map for 2-D Sod test

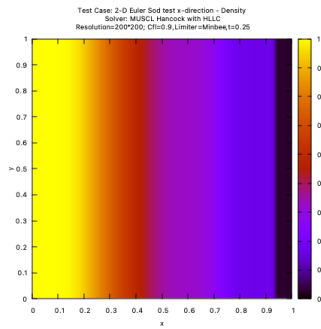


Figure A.30: Density plot from 2-D Sod test with x-split IC

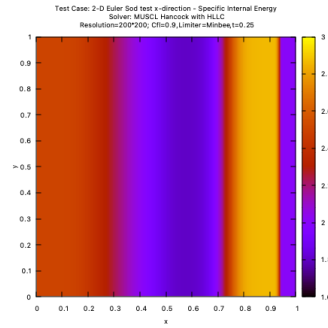


Figure A.33: Specific Internal Energy plot from 2-D Sod test with x-split IC

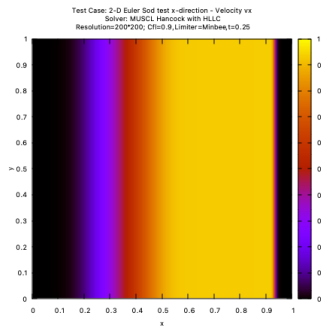


Figure A.31: Velocity vx plot from 2-D Sod test with x-split IC

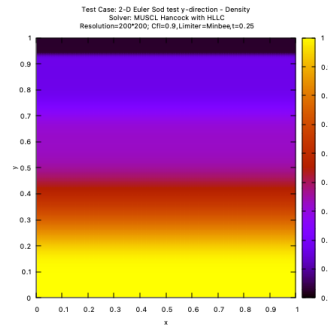


Figure A.34: Density plot from 2-D Sod test with y-split IC

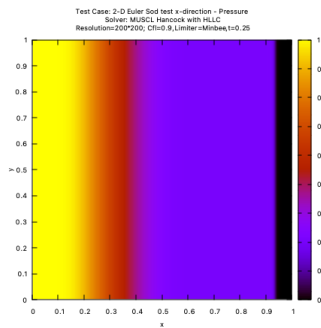


Figure A.32: Pressure plot from 2-D Sod test with x-split IC

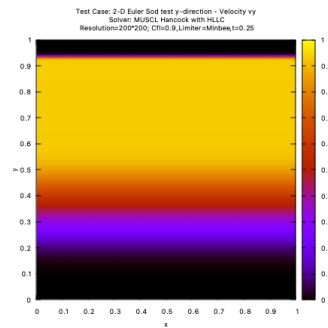


Figure A.35: Velocity vy plot from 2-D Sod test with y-split IC

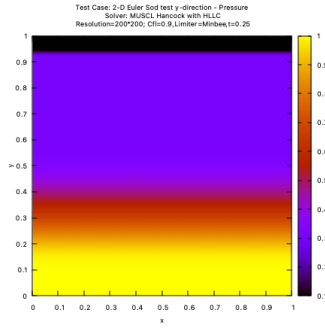


Figure A.36: Pressure plot from 2-D Sod test with y-split IC

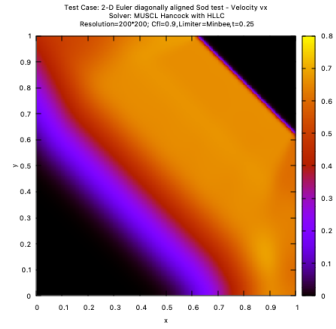


Figure A.39: Velocity vx plot from 2-D Sod test with diagonally aligned IC

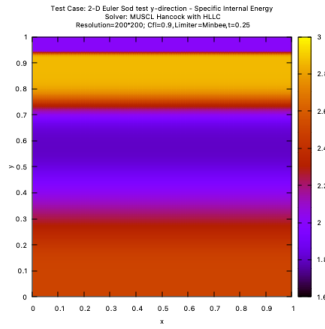


Figure A.37: Specific Internal Energy plot from 2-D Sod test with y-split IC

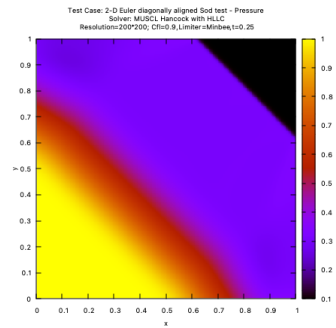


Figure A.40: Pressure plot from 2-D Sod test with diagonally aligned IC

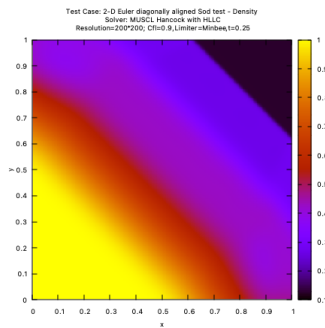


Figure A.38: Density plot from 2-D Sod test with diagonally aligned IC

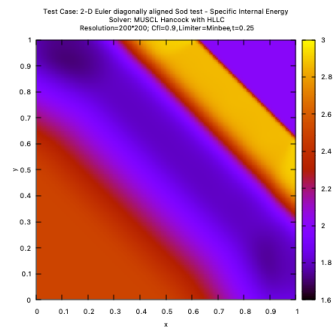


Figure A.41: Specific Internal Energy plot from 2-D Sod test with diagonally aligned IC

Appendix B. Colour map for 2-D Brio and Wu test

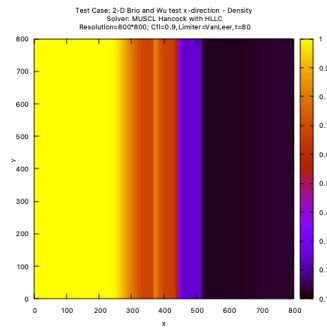


Figure B.42: Density plot from 2-D Brio and Wu test with x-split IC

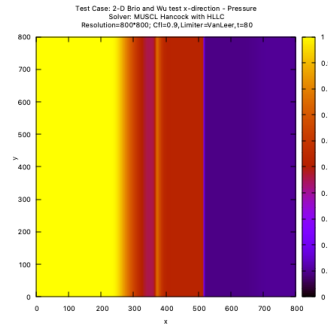


Figure B.45: Pressure plot from 2-D Brio and Wu test with x-split IC

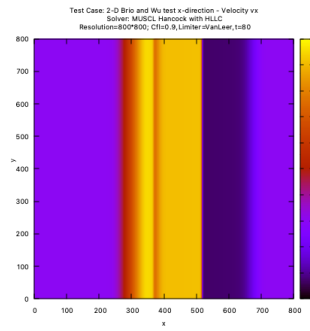


Figure B.43: Velocity vx plot from 2-D Brio and Wu test with x-split IC

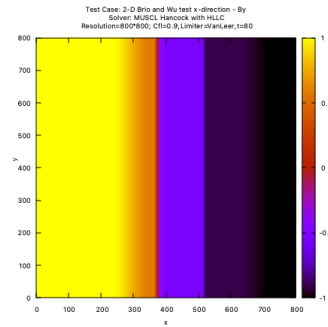


Figure B.46: By plot from 2-D Brio and Wu test with x-split IC

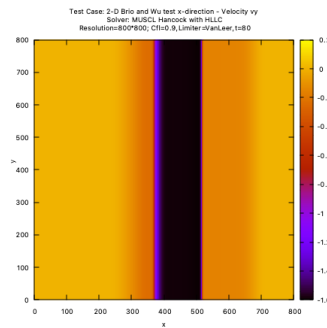


Figure B.44: Velocity vy plot from 2-D Brio and Wu test with x-split IC

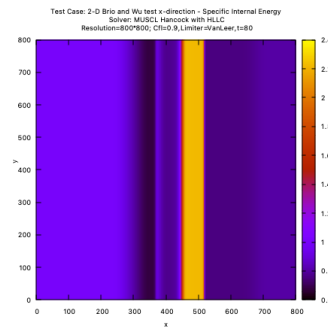


Figure B.47: Specific Internal Energy plot from 2-D Brio and Wu test with x-split IC

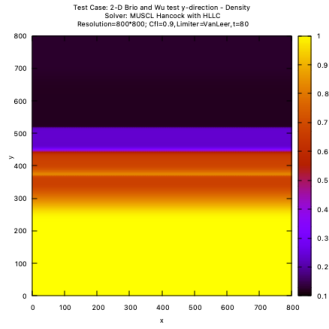


Figure B.48: Density plot from 2-D Brio and Wu test with y-split IC

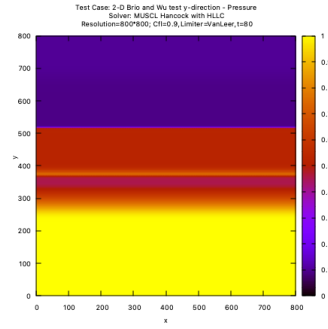


Figure B.51: Pressure plot from 2-D Brio and Wu test with y-split IC

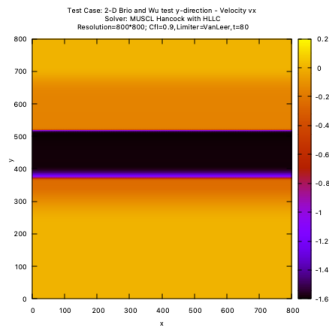


Figure B.49: Velocity vx plot from 2-D Brio and Wu test with y-split IC

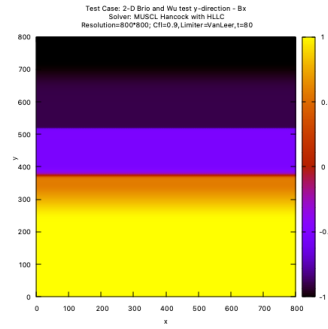


Figure B.52: Bx plot from 2-D Brio and Wu test with y-split IC

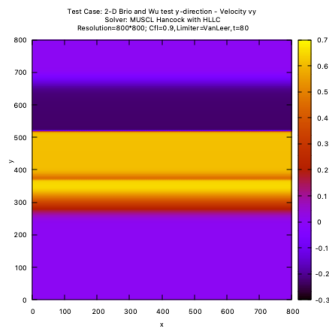


Figure B.50: Velocity vy plot from 2-D Brio and Wu test with y-split IC

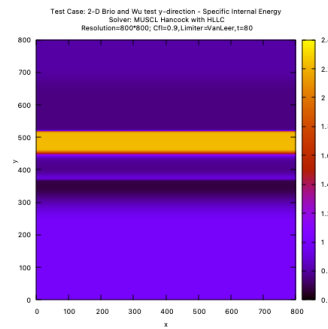


Figure B.53: Specific Internal Energy plot from 2-D Brio and Wu test with y-split IC

References

- [1] Orszag-Tang Vortex Test. www.astro.princeton.edu/jstone/Athena/tests/orszagtang/pagesource.html [Accessed: 2022-03-01].
- [2] M Brio and C.C Wu. An upwind differencing scheme for the equations of ideal magnetohydrodynamics. *Journal of Computational Physics*, 75(2):400–422, 1988.
- [3] F.F. Chen. *Introduction to Plasma Physics*. Springer US, 2012.
- [4] Wenlong Dai and Paul R. Woodward. An approximate riemann solver for ideal magnetohydrodynamics. *Journal of Computational Physics*, 111(2):354–372, 1994.
- [5] A. Dedner, F. Kemm, D. Kröner, C.-D. Munz, T. Schnitzer, and M. Wesenberg. Hyperbolic divergence cleaning for the mhd equations. *Journal of Computational Physics*, 175(2):645–673, 2002.
- [6] Charles R. Evans and John F. Hawley. Simulation of Magnetohydrodynamic Flows: A Constrained Transport Model. , 332:659, September 1988.
- [7] R. J. Goldston and P.H. Rutherford. *Introduction to Plasma Physics*. Introduction to Plasma Physics. Institute of Physics Pub., 1995.
- [8] Katharine Gurski. An hllc-type approximate riemann solver for ideal magnetohydrodynamics. *SIAM JOURNAL ON SCIENTIFIC COMPUTING*, 25:2165–2187, 01 2004.
- [9] ITER. In a few lines, 2022. <https://www.iter.org/proj/inafewlines3> [Accessed: 2022-03-04].
- [10] H. Guillard et B. Nkonga J. Vides, E. Audit. Divergence-free mhd simulations with the heracles code. *ESAIM*, 43:180–194, 2013.
- [11] P. Janhunen. A positive conservative method for magnetohydrodynamics based on hll and roe methods. *Journal of Computational Physics*, 160(2):649–661, 2000.
- [12] Shengtai Li. An hllc riemann solver for magnetohydrodynamics. *Journal of Computational Physics - J COMPUT PHYS*, 203:344–357, 02 2005.
- [13] Timur Linde. A practical, general-purpose, two-state hll riemann solver for hyperbolic conservation laws. *International Journal for Numerical Methods in Fluids*, 40(3-4):391–402, 2002.
- [14] Andrea Malagoli, Gianluigi Bodo, and Robert Rosner. On the Nonlinear Evolution of Magnetohydrodynamic Kelvin-Helmholtz Instabilities. , 456:708, January 1996.
- [15] Stephen Millmore, Louisa Michael, and Nikos Niki-forakis. Lecture notes in advanced continuum modelling, November 2021.
- [16] Takahiro Miyoshi and Kanya Kusano. A multi-state hll approximate riemann solver for ideal magnetohydrodynamics. *Journal of Computational Physics*, 208(1):315–344, 2005.
- [17] Kenneth G. Powell. *An Approximate Riemann Solver for Magnetohydrodynamics*, pages 570–583. Springer Berlin Heidelberg, Berlin, Heidelberg, 1997.
- [18] Kenneth G. Powell, Philip L. Roe, Timur J. Linde, Tamas I. Gombosi, and Darren L. De Zeeuw. A solution-adaptive upwind scheme for ideal magnetohydrodynamics. *Journal of Computational Physics*, 154(2):284–309, 1999.
- [19] Dongsu Ryu, T. W. Jones, and Adam Frank. Numerical Magnetohydrodynamics in Astrophysics: Algorithm and Tests for Multidimensional Flow. , 452:785, October 1995.
- [20] W.B. Thompson. *An Introduction to Plasma Physics*. Elsevier Science, 2013.
- [21] Eleuterio Toro. *Riemann Solvers and Numerical Methods for Fluid Dynamics: A Practical Introduction*. 01 2009.
- [22] M. Wesenberg. Efficient mhd riemann solvers for simulations on unstructured triangular grids. 10(1):37–71, 2002.